Applied Catalysis B: Environmental 165 (2015) 763–773

Contents lists available at ScienceDirect

Applied Catalysis B: Environmental

journal homepage: www.elsevier.com/locate/apcatb

Synthesis of hierarchically porous L-KIT-6 silica–alumina material and the super catalytic performances for hydrodesulfurization of benzothiophene

Aijun Duan[a], Tianshu Li[a,b,1], Zhen Zhao[a,*], Baijun Liu[a,*], Xiaofeng Zhou[a], Guiyuan Jiang[a], Jian Liu[a], Yuechang Wei[a], Huifang Pan[a]

[a] State Key Laboratory of Heavy Oil Processing, China University of Petroleum, Beijing 102249, PR China
[b] Petrochemical Research Institute, China National Petroleum Corporation, Beijing 100195, PR China

ARTICLE INFO

Article history:
Received 16 August 2014
Received in revised form 25 October 2014
Accepted 29 October 2014
Available online 4 November 2014

Keywords:
Micro/mesoporous composite material
Hydrodesulfurization catalyst
L-KIT-6
Benzothiophene
Reaction network

ABSTRACT

A novel micro/mesoporous composite material L-KIT-6 (LK) was successfully synthesized from zeolite L nano-crystals using low cost solid silica–alumina microsphere via two-step hydrothermal crystallization method. LK was used as catalyst support to prepare the hydrodesulfurization (HDS) catalyst. LK micro/mesoporous material and its corresponding catalyst CoMo/LK were characterized using XRD, FTIR, SEM, TEM, N_2-adsorption, ^{27}Al MAS NMR, Pyridine-FTIR, H_2-TPR, XPS and HRTEM techniques. The physicochemical properties of CoMo/LK were compared with the reference catalysts with different support materials including zeolite L, KIT-6 and γ-Al_2O_3. The characterization results demonstrated that the textural and acidic properties of the LK composite were dramatically improved comparing with that of zeolite L and mesoporous silica KIT-6. Furthermore, LK had a positive effect on the formation of moderate MoS_2 stacking morphology and more "edge" active centers. The catalyst CoMo/LK exhibited a superior catalytic performance for HDS of BT, which could be attributed to the synergistic effects of open porous structure, excellent textural property, appropriate acidity, and MoS_2 stacking morphology of CoMo/LK. Moreover, a possible reaction network for BT HDS over CoMo/LK catalyst was proposed.

1. Introduction

With the growing concerns about environmental problems, more stringent fuel specifications have been carried out in numerous countries to constraint sulfur contents in gasoline (<10 ppm) [1]. To reach this ultra low sulfur content, highly refractory sulfur compounds in gasoline fraction, such as alkylthiophene and benzothiophene (BT) must be desulfurized [2]. Conventional alumina-supported Co(Ni)Mo industrial hydrodesulfurization (HDS) catalysts fail to achieve the ultra-low sulfur standard due to the single Lewis acid sites distribution and amorphous pore structures of Al_2O_3. In order to develop high-efficiency HDS catalysts, several approaches including preparation method, selection of supports and active components have been pursued among which the development of novel catalyst support materials is of great importance.

A wide variety of support materials such as zeolite NaY [3], basic magnesium oxides [4], amphoteric carbon [5] and mesoporous materials [6–8] have been employed as candidate supports for the partial or complete substitution of conventional support γ-Al_2O_3. Due to strong acidity, high stability and shape selectivity, acidic zeolites are widely used as the supports for HDS catalysts. The synergistic effect of different acid sites not only accelerates the direct cleavage of the C—S bond but also promotes alternative pathways to remove the sulfur atom attached to the aromatic rings. Zeolite L possesses a LTL type framework topology with one-dimension pore channels and shows excellent catalytic performances in the selective hydrogenation [9] and HDS [10]. However, similar to other zeolites, the small pore size (0.71 nm × 0.71 nm) of zeolite L strongly hinders the diffusion of bulky molecules after loading of MoS_2 active phase [11].

Mesoporous materials with outstanding textural characteristics including large specific area and open porosity are considered to be an ideal catalyst supports for catalytic conversion of bulky molecules. KIT-6, a type of bicontinuous cubic $Ia\bar{3}d$ mesoporous

* Corresponding authors at: State Key Lab of Heavy Oil Processing, China University of Petroleum, College of Science, Beijing 102249, China.
Tel.: +86 10 89731586/+86 10 89733751; fax: +86 10 69724728.
E-mail addresses: zhenzhao@cup.edu.cn (Z. Zhao), bjliu@cup.edu.cn (B. Liu).
[1] This author has equal contribution as the first author.

http://dx.doi.org/10.1016/j.apcatb.2014.10.078
0926-3373/

material, possesses large specific surface area and large pores sizes which could enhance the dispersion and the accessibility of active centers [12]. Soni et al. [13] used KIT-6 material as CoMo catalyst support for the HDS of thiophene and the corresponding catalyst exhibited a higher activity than SBA-15 and γ-Al_2O_3-supported catalysts. Larger pore size and excellent interconnected framework structure of KIT-6 might be the reasons for its high activity. Nevertheless, the weak acidity and stability restrict its applications in catalytic area.

In order to combine the advantages of microporous zeolites and mesoporous silica materials, many considerable efforts have been devoted to synthesizing novel zeolite with mesostructure. Various mesoporous zeolites were synthesized and applied in the catalytic processes. Sirvastava et al. [14] reported that MFI zeolite with a hierarchical porous structure (MeMFI) exhibited relatively high activities in the catalytic synthesis of bulky molecules and improved the catalytic stability in reactions involving small molecules. The high activities of these catalysts were related to the mesoporous/microporous structure and mild acidity of MeMFI. Di [15] firstly synthesized ordered mesoporous aluminosilicates of MAS-3 and MAS-8 from L precursors, which retained the similar structures to MCM-41 and SBA-15, respectively. MAS-8 showed a higher conversion than the mesoporous aluminosilicates Al-MCM-41 and Al-SBA-15 in the cumene cracking process, which was ascribed to the improvement of acidity derived from L precursors.

Due to the desired properties, micro/mesoporous composite materials have become the focus of HDS catalysts. Sun [16] reported a high activity in the HDS of 4, 6-dimethyldibenzothiophene (4,6-DMDBT) over noble metals supported on mesoporous ZSM-5 zeolite. Fu [17] prepared mesoporous zeolite Y catalysts (Pd/HY-M), and this catalyst showed a very high activity in the HDS of 4, 6-DMDBT compared with Pd/HZSM-5-M, Pd/HBeta-M and Pd/γ-Al_2O_3. This high activity could be attributed to the combination of the advantages for the mesoporosity and large pore size in HY-M. In our previous works [18,19], zeolite Beta and L-based composite materials with the characteristic mesostructures of KIT-6 and MCM-41 were prepared, respectively. The corresponding catalysts exhibited better HDS efficiency than their counterpart catalysts using single zeolites and mesoporous materials as supports. It can be concluded that the supports with open porous structure and appropriate acidic properties would make positive effects on enhancing HDS activities of catalysts.

In the present work, a novel micro/mesoporous composite material L-KIT-6(LK) was firstly synthesized by a two-step hydrothermal crystallization method using low-cost solid silica–alumina microspheres. The corresponding CoMo supported catalyst CoMo/LK was prepared and evaluated in the HDS of benzothiophene. To investigate the effects of textural and acidity of supports on the catalytic performances, other catalysts with different support materials including zeolite L, KIT-6 and γ-Al_2O_3 were also evaluated for comparison. Various techniques were employed to characterize both physicochemical properties of supports and corresponding catalysts. The main factors affecting the catalytic performance of LK composite supported CoMo catalyst for the HDS of benzothiophene were discussed. Furthermore, a possible reaction network of benzothiophene HDS over the CoMo/LK catalyst was proposed.

2. Experimental

2.1. Synthesis of materials

The micro/mesoporous composite material L-KIT-6 (LK) was hydrothermally synthesized from the in-situ assembly of $EO_{20}PO_{70}EO_{20}$ (Pluronic P123, M_{av} = 5800, Aldrich) with a preformed L microcrystal solution. First, zeolite L nanocrystal clusters were prepared with the molar ratio of 1.0 SiO_2:0.1 Al_2O_3:0.15 K_2O:25·H_2O. A kind of low-cost silica–alumina microsphere (Fushun Catalyst Company, SiO_2 69.4 wt%, Al_2O_3 11.8 wt%) was used as the silica and aluminum sources, then it was mixed with an aqueous solution of KOH (Beijing Chemical Company, 82 wt%). The mixture was homogenized by stirring for 1 h, followed by transferring the material into a Teflon-lined autoclave for crystallization at 150 °C for 10 h. The zeolite with L nanocrystal clusters were obtained as precursor. Second, 2 g Pluronic P123 was dissolved in the mixture of H_2O and hydrochloric acid solution at 35 °C. After complete dissolution, 3.94 g *n*-butanol was added and the mixture was stirred for 1 h. Then a certain amount of the mixture with the precursor zeolite L species and TEOS was added to the above solution with vigorous string, resulting a gel of SiO_2:Al_2O_3:P123:*n*-butanol:HCl:H_2O with a molar ratio of 1:0.05:0.015:1.4:2.3:215. The mixture was stirred at 35 °C for 24 h and transferred into a Teflon-lined autoclave at 100 °C for 24 h under static conditions. The resulting solid product was collected by filtration, washed, dried and calcined at 550 °C for 6 h in air to remove the organic template.

Zeolite L was synthesized as mentioned above, but the crystallization time of zeolite L was extended to 24 h. KIT-6 and Al-KIT-6 were prepared according to the published literature [12,20].

2.2. Preparation of catalysts

H-type materials of zeolite L and composite material L-KIT-6(LK) were obtained by ion-exchanged with a 1.0 M NH_4Cl aqueous solution at 90 °C for 1 h. Then they were washed and calcined at 550 °C in air for 4 h.

The corresponding catalysts with different supports (γ-Al_2O_3, zeolite L, KIT-6 and L-KIT-6(LK)) were prepared by a two-step incipient-wetness impregnation of ammonium molybdate and cobalt nitrate as active metal components separately. After each impregnation, the samples were dried at 110 °C for 12 h and calcined at 550 °C for 4 h in air to yield oxidic catalysts. All the samples were impregnated with the same loadings of 8 wt% MoO_3 and 4 wt% CoO. Then the obtained samples were crushed into 0.3–0.5 mm particles. According to the supports, the resulting catalysts were denoted as CoMo/Al_2O_3, CoMo/L, CoMo/KIT-6 and CoMo/LK. Table S1 lists the nominal component ratio of catalysts and the contents of MoO_3 and CoO of different catalysts determined by ICP-OES method. Both MoO_3 and CoO contents are close to the nominal ones (8 and 4 wt%, respectively).

2.3. Characterization of the supports and catalysts

X-ray powder diffraction (XRD) patterns of the samples were recorded with a Shimadzu X-6000 diffraction Cu *K*α radiation. For small angle scans, the 2θ range was from 0.7° to 5° (the diffractometer was operated at 250 mA), and for wide angle scans, from 5° to 80° (the diffractometer was operated at 30 mA).

Fourier transform infrared spectroscopy (FTIR) absorbance spectra were performed in the wave numbers range from 4000 to 400 cm^{-1} on a MAGNA-IR 560 spectrophotometer. The transparent discs were pressed using 2 mg of the samples mixed with 200 mg of KBr.

Nitrogen adsorption–desorption isotherms were measured in a Quantachrome Autosorb-iQ automated gas sorption analyzer at 77 K. The specific surface areas of the samples were calculated using the Brunauer–Emmett–Teller (BET) method. The total volumes of micro- and mesopores were calculated from the amounts of nitrogen adsorbed at p/p_o = 0.98. The pore size distribution (PSD) was derived from the desorption branches of the isotherms using the Barrett–Joyner–Halenda (BJH) method. Nonlocal density functional

theory (NLDFT) analyses were performed to evaluate the PSD of the cubic $Ia\bar{3}d$ materials. For the analyses, the kernel of NLDFT equilibrium capillary condensation isotherms of N_2 at 77 K on silica was selected as the model isotherm (using desorption branch and assuming cylindrical pores). The micropores were determined from the *t*-plot analysis.

Transmission electron microscopy (TEM) images were performed with a JEOL JEM 2100 electron microscope operated at an accelerating voltage of 200 kV. The samples were milled firstly in an agate mortar and ultrasonically suspended in ethanol. A drop of the supernatant liquid was placed on a copper grid coated with a sputtered carbon polymer.

Scanning electron microscopy (SEM) analyses were conducted on a Cambridge S-360 instrument operating at 20 kV. The samples were coated with gold prior to SEM measurements.

^{27}Al solid-state magic-angle-spinning nuclear magnetic resonance (MAS NMR) spectra were recorded on a Bruker MSL-300NMR spectrometer with frequency at 59.6 MHz, pulse width at 4.5 ms, and delay at 30 s.

Surface acid amounts and types of the samples were obtained by a pyridine-FTIR(Py-FTIR) spectroscopy on a MAGNAIR 560 FTIR instrument with a resolution of 1 cm^{-1}. The samples were dehydrated at 500 °C for 5 h under a vacuum of 1.33×10^{-3} Pa, followed by adsorption of purified pyridine vapor at room temperature for 20 min. The system was then degassed and evacuated at different temperatures, and the IR spectra were recorded.

H_2 temperature-programmed reduction (H_2-TPR) analysis was carried out in a conventional flow apparatus. 100 mg sample was pretreated under air atmosphere by calcination at 200 °C for 1 h and subsequently cooled to 30 °C. Afterwards, 10% H_2/Ar flow (40 mL min^{-1}) was passed over the catalyst bed while the temperature was ramped from 30 to 900 °C at a heating rate of 10 °C min^{-1}. The hydrogen consumption signal was monitored by a thermal conductivity detector (TCD).

High resolution transmission electron microscopy (HRTEM) images of the sulfided CoMo supported catalysts were obtained on a Philips Tecnai G2 F20 transmission electron microscope operated at an accelerating voltage of 200 kV. The oxidic catalysts were first sulfided in a 2 wt% CS_2/cyclohexane stream at 340 °C for 4 h, cooled to room temperature in a N_2 flow and then kept in alcohol to prevent oxidation.

X-ray photoelectron spectroscopy (XPS) measurements of the sulfided catalysts were measured and recorded on a VG ESCA Lab 250 spectrometer using Al *K*α radiation. Before measurement, the sample to be tested was pressed onto a stainless steel sample holder and then the holder was immediately mounted on the XPS machine.

2.4. Catalytic performance evaluation

The HDS activities evaluation of benzothiophene (BT) over CoMo/Al_2O_3, CoMo/L, CoMo/KIT-6 and CoMo/LK catalysts were tested in a high-pressure fixed-bed microreactor using 0.2 wt% BT in cyclohexane as a model compound. The 0.5 g catalyst was presulfided for 4 h with 2 wt% CS_2-cyclohexane and H_2 mixture at 320 °C, 2 MPa, liquid hourly space velocity (LHSV) of 1.0 h^{-1}, and H_2/cyclohexane ratio of 300 mL mL^{-1}. After presulfidation, HDS reactions were conducted under the conditions of temperature 270 °C, 2.0 MPa, and H_2/model compound ratio of 200 mL mL^{-1}. The liquid product was collected after reaching the steady state. The sulfur contents in the reactant and product were measured by a RPP-2000SN sulfur & nitrogen analyzer (Taizhou Central Analytical Instruments Co. Ltd. P.R. China). The reaction products of BT HDS were analyzed by an offline Finnigan Trace GC/MS with an HP-5MS capillary column (30 m × 0.25 mm × 0.25 μm) and a pulsed flame photometric detector (PFPD). Assuming a pseudo-first-order reaction for BT HDS, the catalytic activity was determined by the following equation [21]:

$$k_{HDS} = \frac{F}{m} \ln\left(\frac{1}{1-\tau}\right) \quad (1)$$

where *F* is the feeding rate of the reactant in mol h^{-1}, *m* is the catalyst mass in grams, and τ is the total conversion of BT, and k_{HDS} is the rate constant of BT HDS in mol g^{-1} h^{-1}. In addition, the BT HDS rate was also calculated in terms of a parameter of turnover frequency, TOF (h^{-1}), defined as the number of desulfurized BT molecule per hour and per catalytic site. Different types of active sites (basal plane of sulfides, sulfur vacancies, promoted CoMo sites, etc.) are presumably present on the HDS catalysts. The TOFs (h^{-1}) of different catalysts were calculated by considering of the edge sites [6,22,23]. In the present work, we used the Mo atoms on the edges of MoS_2 crystallites as catalytic sites. For the supported MoS_2 HDS catalysts, Eq. (2), which is widely used to estimate the relative proportion of Mo atoms per crystallite, can be recommended as a good estimate of TOF [24].

$$f_{Mo} = \frac{Mo_{edge}}{Mo_{total}} = \frac{\sum_{i=1}^{t}(6ni-6)}{\sum_{i=1}^{t}3ni^2-3ni+1} \quad (2)$$

where n_i is the number of the Mo atoms along one side of a MoS_2 slab determined from its length ($\bar{L} = 3.2(2n_i - 1)$ Å) and *t* is the total number of slabs shown by HRTEM micrographs. Here, it is assumed that all the edge sites are active for HDS reactions, so the real value of f_{Mo} could be higher than the estimated one from Eq. (2).

3. Results and discussion

3.1. Characterization of supports and catalysts

3.1.1. X-ray diffraction and ICP-OES characterization

The low-angle XRD patterns of KIT-6 and LK are shown in Fig. 1A. The samples of KIT-6 and LK exhibit a well-distinguished diffraction peak at $2\theta = 0.81°$ and 0.87° corresponding to (2 1 1) plane and a hump for (2 2 0) plane at $2\theta = 0.94°$ and 1.0, correspondingly. The d_{211} of the KIT-6 and LK samples are 105.4 and 103.8 nm, respectively. The unit cell parameter a_o of the KIT-6 and LK samples which are calculated from $a_o = 6^{1/2}d_{(211)}$ to be 25.8 and 25.4 nm, in consistent with the previous report [12]. In wide-angle domain (Fig. 1B), LK exhibits a series of characteristic peaks at $2\theta = 5.5°$, 19.4°, 22.7°, 28.0°, 29.1°, and 30.7° which can be assigned to the LTL topological structure of zeolite L [25]. These results of micro/mesoporous material LK agree well with the structure characteristics of mesoporous material KIT-6 and zeolite L, implying that LK possesses the similar structure to both of the body-centered cubic $Ia\bar{3}d$ space group and LTL topology.

The results of powder XRD of the CoMo oxide catalysts using different support materials are displayed in Fig. 2. It can be clearly found that both CoMo/KIT-6 and CoMo/LK exhibit the same characteristic peaks of mesoporous material KIT-6 in Fig. 2A, suggesting that the mesoporous cubic structure are retained after the impregnation of active metals. The intensities of characteristic peaks decrease, which are probably due to the loss of long range order of the support mesostructure induced by a partial blocking of its pore channels by Co and Mo oxidic species. For the catalysts CoMo/L and CoMo/LK, the diffraction peaks ascribed to zeolite L between 5° and 35° are observed. For the CoMo/Al_2O_3 catalyst, several obvious peaks $2\theta = 19.4°$, 37.6°, 45.8°, and 67.0° belonged to γ-Al_2O_3 can be seen. Beyond that, no obvious XRD diffraction peaks correlated to the MoO_3 crystal at $2\theta = 23.3°$ and 27.3° are detected in the all catalysts, implying that MoO_3 and CoO components have high dispersion degree over the support surfaces [13]. Three characteristic

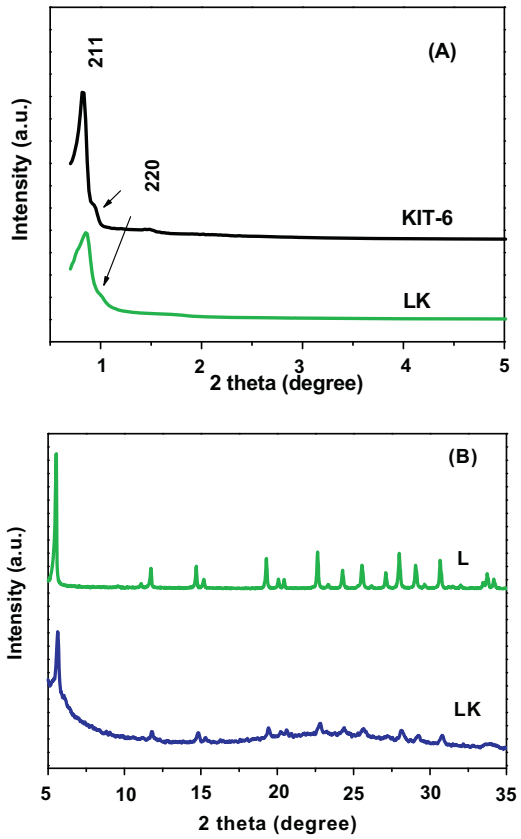

Fig. 1. XRD patterns of the as-synthesized materials. (A) low-angle domain; (B) wide-angle domain.

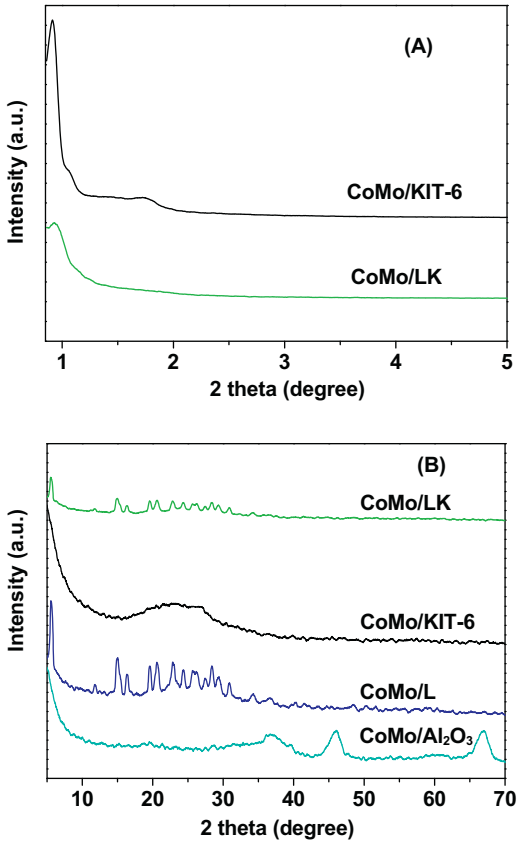

Fig. 2. XRD patterns of the corresponding supported CoMo catalysts. (A) low-angle domain; (B) wide-angle domain.

peaks appear at $2\theta = 36.8^\circ$, 46.2° and 66.7° are attributed to γ-Al_2O_3 in the wide angle domain of CoMo/Al_2O_3.

3.1.2. FTIR spectroscopy results

The FTIR spectra of zeolite L, KIT-6 and LK in the region of 400–900 cm^{-1} are displayed in Fig. S1. In the spectrum of zeolite L, IR bands centered at ~608 and 470 cm^{-1} are attributed to the characteristic vibration bands of 5-ring and 6-ring T—O—T [19], and the bands centered at ~775 and 729 cm^{-1} are assigned to the external and internal symmetric stretching bands of TO_4, respectively [26]. The pure silica phase KIT-6 sample shows the bending and symmetric stretching vibrations bands of Si—O—Si centered at ~470 and 807 cm^{-1} [27]. Composite material LK gives the distinguished bands centered at ~610, 729 and 775 cm^{-1} belonging to zeolite L, moreover, the characteristic band of KIT-6 centered at ~807 shifts to 794 cm^{-1} over LK composite which can be attributed to the co-effective result of the framework vibration of zeolite L and KIT-6. These results illustrate that mesoporous walls or matrix of LK contain the primary and secondary building units of zeolite L, which can not only improve the pore structural stability, but also adjust the acidity property of the LK composite. These results are consistent with the XRD results.

3.1.3. Morphology of the supports

The SEM images of the as-synthesized samples are presented in Fig. S2. The SEM image of zeolite L possesses a cylindrical morphology with substantially flat basal planes and with the cylinder length of ~1.2 μm [28] (Fig. S2A). Mesoporous material KIT-6 shows an agglomeration of irregular particles (Fig. S2B). No obvious difference in particle morphology between the KIT-6 and Al-KIT-6 materials (Fig. S2C) is observed. Comparing with KIT-6, the SEM image (Fig. S2D) of LK also displays irregular particles morphology, but with much smaller particle size. Moreover, no zeolite L nanoparticles are observed in the SEM image of LK, indicating that zeolite L nanocrystals are finely assembled into the mesoporous framework.

TEM images of the as-synthesized samples are shown in Fig. 3. LTL topology structure of zeolite L is difficult to discern the micrograph. The TEM images of KIT-6, Al-KIT-6 and LK display the representative characteristic ordered cubic $Ia\bar{3}d$ symmetric mesostructure with well-ordered cubic arrays of the pores along (3 1 1) reflection, and the images are similar to those reported KIT-6 materials previously [29]. However, the micro/mesoporous material prepared from zeolite L nanoclusters is not as ordered as KIT-6. This phenomenon can be attributed to the nanoclustered silicon species that have stronger rigidity and larger volumes than those nanostructured silicon species used in the conventional synthesis of KIT-6. The assembly of these zeolite nanoclusters is relatively difficult and needs more space to connect with each other, which results in a thicker wall and somewhat disorder in the synthesized products [30]. These observations agree well with the results of N_2 adsorption and XRD results.

3.1.4. Porous properties of the materials and catalysts

The porous properties of the as-synthesized materials and their corresponding CoMo supported catalysts were investigated by N_2 adsorption. The isotherms and pore size distribution (PSD) curves of the materials and corresponding catalysts are shown in Fig. 4 and Fig. S3, respectively. In Fig. 4, similar to the mesoporous silica KIT-6, the micro/mesoporous composite material LK exhibits type IV isotherm with H1 type hysteresis loop and a narrow mesoporous distribution, which are the typical behaviors of the ordered mesostructures. Moreover, the composite material LK also displays the characteristic of the microporous material of zeoliet L with a distinct adsorption amount at low relative pressure ($p/p_o < 0.02$). But the height of hysteresis

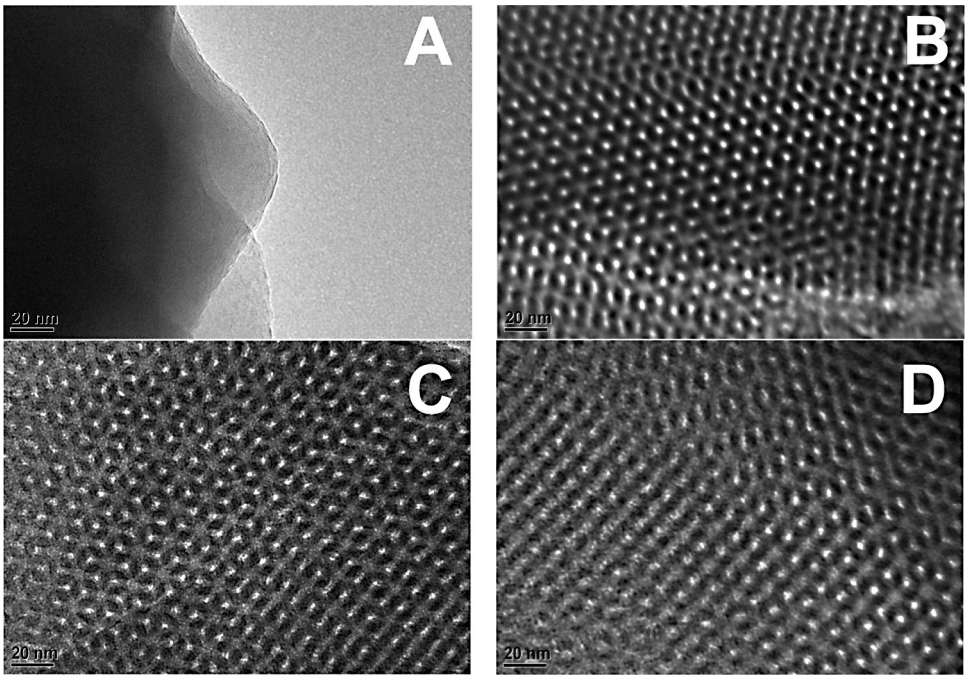

Fig. 3. TEM images of the as-synthesized materials. (A) L; (B) KIT-6; (C) Al-KIT-6; (D) LK.

loop of LK decreases, reflecting a loss of pore volume compared with that of KIT-6. Zeolite L displays type I isotherm of microporous material and no mesopore is observed in its PSD curve. Al_2O_3 shows a H4 type hysteresis loop and a broad pore diameter distribution, which can be attributed to the inter-particle space.

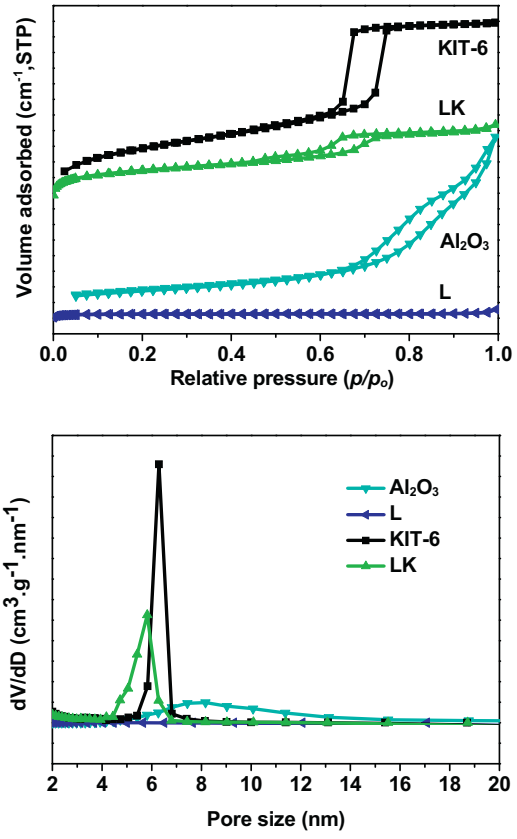

Fig. 4. N_2 adsorption–desorption isotherms and BJH pore diameter distributions patterns of the as-synthesized materials.

The nitrogen adsorption–desorption isotherms and PSD curves of the corresponding catalysts are shown in Fig. S3. All the catalysts used different materials as supports exhibit similar isotherms compared with those of parent materials, except for the decreasing heights of the hysteresis loop after loading of the active metals due to the loss of pore volume resulting from metal deposition. The mean PSD curves show no significant decreases in intensities after the impregnation of metals, which confirm that the mesostructures of different materials are reserved.

The textural properties of the as-synthesized materials and the corresponding supported CoMo catalysts are summarized in Table 1. KIT-6 shows the largest specific surface area, pore volume and mean pore diameter. Comparing with that of KIT-6, the counterpart pore diameter, specific surface area and total pore volume of LK show a decreasing tendency. This phenomenon can be explained by the pore plugging inside mesoporous channels due to the assembly of some non-uniform size nanocrystals of zeolite L. Moreover, the presence of nanocrystal zeolite L in the mesoporous wall contributes to larger micropore volume (0.11 $cm^3\ g^{-1}$) of LK than that of KIT-6 (0.03 $cm^3\ g^{-1}$). LK shows better textural properties than zeolite L, implying that the introduction of mesoporous template can markedly improve the textual properties of the composite material. The pore wall thickness of LK (5.5 nm) is greater than that of KIT-6 (5.3 nm). This is probably attributed to the assembly of the primary and secondary building units of zeolite L into the LK mesoporous wall, which not only favor the improvement of mesoporous phase stability [31], but also combine the benefits of acidity and mass transfer. The significant losses of specific surface areas and pore volumes of the counterpart catalysts are observed over the catalysts in comparison with all the corresponding support materials. The microstructure and small pore size of zeolite L result in the highest textural losses over CoMo/L. Relatively smaller amount textural losses are also observed on the CoMo/KIT-6 and CoMo/LK, which can be explained by the mesostructure and larger pore sizes of mesoporous and micro/mesoporous composite materials.

Table 1
Textural properties of different materials and the counterprat supported catalysts.

Sample	S_{BET}[a] ($m^2\ g^{-1}$)	V_t[b] ($cm^3\ g^{-1}$)	V_{mes}[c] ($cm^3\ g^{-1}$)	V_{mic}[d] ($cm^3\ g^{-1}$)	a_o[e] (nm)	d_{BJH}[f] (nm)	d_{DFT}[g] (nm)	b_w[h] (nm)
Al_2O_3	239	0.89	0.86	–	–	8.2	–	–
L	352	0.16	–	0.13	–	0.6	–	–
KIT-6	795	0.99	0.97	0.03	25.8	6.3	7.6	5.3
LK	493	0.54	0.44	0.11	25.4	5.8	7.3	5.5
CoMo/Al_2O_3	181	0.59	0.58	0.01	–	7.8	–	–
CoMo/L	89	0.09	0.08	0.01	–	–		–
CoMo/KIT-6	369	0.57	0.56	0.03	–	6.3		–
CoMo/LK	226	0.32	0.28	0.04	–	5.8		–

[a] Calculated by the BET method.
[b] The total pore volume was obtained at a relative pressure of 0.98.
[c] Calculated using the BJH method.
[d] Calculated using the *t*-plot method.
[e] XRD unit cell parameter (a_o) was estimated from $a_0 = 6^{1/2} d_{211}$ [10].
[f] Mesopore diameter calculated using the BJH method.
[g] Mesoporous diameter calculated by the DFT method using the kernel of NLDFT equilibrium capillary condensation isotherms of N_2 at 77 K on silica.
[h] Wall thickness evaluated according to Ref. [10], $b_w = a_0/2 - d_{DFT}$.

3.1.5. Al coordination structures

The existence states of Al species in the as-synthesized materials were studied by solid-state ^{27}Al MAS NMR, and the results are shown in Fig. 5. The spectrum of Al-KIT-6 presents two distinct peaks at 54.3 and 0 ppm. The former signal at 54.3 ppm can be assigned to the aluminum species in a tetrahedral framework environment, in which aluminum is covalently bound to four Si atoms via oxygen bridges. The other peak with low intensity at 0 ppm can be attributed to the non-framework Al species with octahedral coordination in the form of polymeric oxo-hydroxo-Al-cations [32]. Zeolite L shows only one peak belonging to the tetrahedral coordination framework aluminum species at 59.4 ppm [33], indicating that all the aluminum species are embeded in the zeolite framework. In the spectrum of LK, the chemical shift of the tetrahedral aluminum species appears around 60.3 ppm, which is close to zeolite L rather than the tetrahedral aluminum at ~54.3 ppm in Al-KIT-6. This observation proves that the mesoporous framework of LK is assembled by zeolite L nanocrystals. The chemical shift at around 0 ppm of LK confirms the existence of non-framework Al species, which are probably generated by the dissolution and dealumination of L nanocrystal in the second step of the synthesis process.

3.1.6. Surface acidity measurement

The acidity properties of the catalysts are measured by Py-FTIR and the results are shown in Fig. S4 and Table 2. The bands located at 1540 and 1450 cm^{-1} can be assigned to pyridine adsorbed on Brönsted (B) and Lewis (L) acid sites, respectively, and the band at 1490 cm^{-1} can be ascribed to pyridine co-adsorbed on both B and L acid sites [34]. As can be seen from Table 2, the amount of total acid sites increases in the order of CoMo/KIT-6 < CoMo/Al_2O_3 ≈ CoMo/LK < CoMo/L. Owing to electronically neutral frameworks of pure silica KIT-6, CoMo/KIT-6 exhibits the lowest acidity amount after the impregnation of active metals. CoMo/L shows the highest amounts of B and L acid sites in all the catalysts, due to the acidity of zeolite L. No B acid sites are detected in CoMo/Al_2O_3 and CoMo/KIT-6. The existence of B and L acid sites is widely recognized to be associated with framework and extra-framework Al species of the zeolites, respectively [35]. Comparably, due to the in-situ assembly of microporous zeolite L, both of acid types and acid amount of CoMo/LK are regulated by LK. Compared with CoMo/L, the lower acid amount of CoMo/LK can be attributed to the partly dealumination of zeolite L nanocrystal during assembling mesostructure under acidic condition. The Py-FTIR results are consistent well with those of ^{27}Al MAS NMR. The moderate acid strength and an appropriate acid-type distribution of CoMo/LK are expected to be responsible for enhancing the synergistic effect between B and L acids, thus improving the catalytic performances.

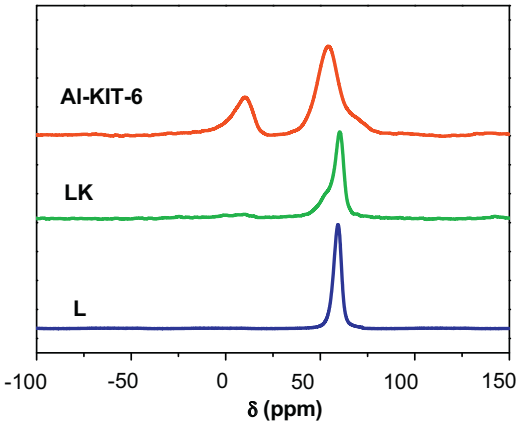

Fig. 5. ^{27}Al MAS NMR spectra of the as-synthesized materials.

3.1.7. H_2-TPR characterization

H_2-TPR characterization gives information about the reducibility of active metals on the catalysts. It is an effective method to characterize metal-support interaction(MSI). The H_2-TPR curves of CoMo/Al_2O_3, CoMo/L, CoMo/KIT-6 and CoMo/LK are shown in Fig. 6. The profiles of all catalysts exhibit two similar characteristic peaks in the ranges of 400–600 and 600–900 °C. The low-temperature reduction peak is assigned to the first step of Mo reduction ($Mo^{6+} + 2e^- \rightarrow Mo^{4+}$) of polymeric octahedral species. The high-temperature reduction peak at around 600 °C can be associated with the complete reduction ($Mo^{4+} + 2e^- \rightarrow Mo^0$) of polymeric octahedral, tetrahedral and bulk crystalline MoO_3 [36]. The highest reduction temperatures of octahedral and tetrahedral Mo species over CoMo/Al_2O_3 catalyst, indicate that Mo species are stabilized and hard to be reduced and sulfided on alumina. Compared with CoMo/Al_2O_3, the reduction temperatures of CoMo/L only slightly decreased a little. The strong interaction via Al—O—Mo

Table 2
Surface acid amounts and acid types of the counterpart supported catalysts.

Catalyst	Acid amount (200 °C) (μmol g^{-1})			Acid amount (350 °C) (μmol g^{-1})		
	L	*B*	*L+B*	*L*	*B*	*L+B*
CoMo/Al_2O_3	205.1	0	205.1	87.3	0	87.3
CoMo/L	263.3	43.3	306.5	119.1	28.2	147.3
CoMo/KIT-6	79.5	0	79.5	29.9	0	29.9
CoMo/LK	197.1	35.3	232.4	79.7	17.6	97.3

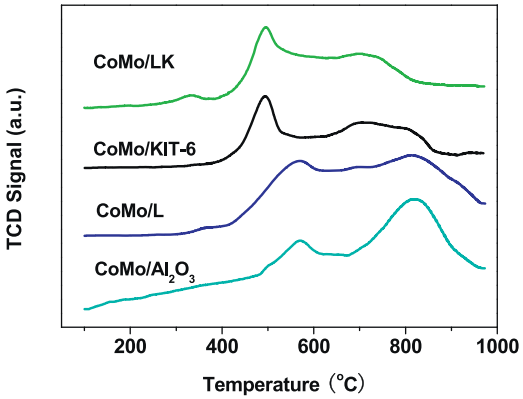

Fig. 6. H_2-TPR profiles of the supported CoMo catalysts.

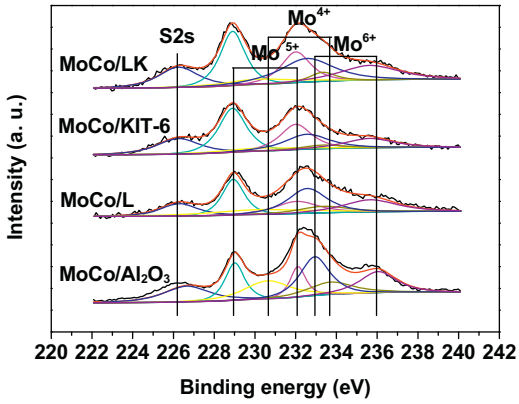

Fig. 7. Mo3d XPS spectra of the sulfided supported CoMo catalysts.

linkages makes Mo species on the zeolite are hard to be reduced and sulfided [37]. Compared with CoMo/L and CoMo/Al_2O_3, a considerable decrease in the high reduction temperature of tetrahedral Mo species and a strong increase in the hydrogen consumption in low temperature region are observed for CoMo/LK. An increase in the proportion of the dispersed octahedral Mo species which are easy to be reduced at the expense of tetrahedral ones indicates weaker MSI over CoMo/LK [38,39]. This relatively weaker MSI originates from the losses of some alumina species of zeolite L nanocrystal clusters under the acidic condition. CoMo/KIT-6 catalyst shows the lowest reduction temperature of Mo species. The less active hydroxyl groups attached to Si in the KIT-6 support is the main reason. The above results show that the MSI of different catalysts increased in the order of CoMo/KIT-6 < CoMo/LK < CoMo/L < CoMo/Al_2O_3. The existence of zeolite L nanocrystal creates more active Al—OH groups which will further interact with Mo species to generate Al—O—Mo bonds, stronger linkage than Si-O-Mo bonds [40]. This leads to the appearance of highly dispersed octahedral and tetrahedral Mo species. The CoMo/LK not only has better dispersion of active metal oxides than KIT-6, but also has much weaker MSI than CoMo/L and CoMo/Al_2O_3. Furthermore, different accessibilities of the surface Si—O—Mo and Al—O—Mo groups also affect the reduction of the metal species. The moderate MSI over CoMo/LK catalyst would benefit the reduction and sulfidation of Mo species, moreover, it probably favors the modulation of the stacking morphology of MoS_2 and the formation of a mixed Co—Mo—S phase [38].

3.1.8. XPS characterization

Since the sulfidation degree of the active metal can significantly influence the HDS efficiency of Mo-based catalysts, XPS characterization measurements were carried out and the Mo 3d XPS spectra and their deconvolution results of the sulfided catalysts are shown in Fig. 7. The binding energies of the Mo $3d_{5/2}$ and Mo $3d_{3/2}$ levels for Mo^{4+} (MoS_2) are about 228.9 and 231.7 eV, respectively, while those for Mo^{5+} (MoOS) are about 230.2 and 233.5 eV, and for Mo^{6+} (MoO_3) are 232.5 and 235.8 eV [41]. The sulfidation degree of the oxidic Mo species, $Mo_{sulfidation}$, which is defined as the ratio of Mo^{4+} to the sum of Mo^{4+}, Mo^{5+} and Mo^{6+} [42] are listed in Table 3. For the above samples, the calculated $Mo_{sulfidation}$ on CoMo/Al_2O_3, CoMo/L, CoMo/KIT-6 and CoMo/LK are 25.90%, 35.26%, 57.42% and 45.62%, respectively. The XPS results demonstrate that Mo species over CoMo/KIT-6 catalyst are easily sulfided compared with other catalysts. This maximum $Mo_{sulfidation}$ can be associated with the weakest MSI results from Si—OH groups with less activity. This benefits the formation of type II Co—Mo—S phase, which are more active than type I Co—Mo—S phase. The catalyst CoMo/L with zeolite L as support has the lower Mo sulfidation degree compared with CoMo/KIT-6 and CoMo/LK catalysts, due to its stronger MSI. CoMo/Al_2O_3 presents the lowest Mo sulfidation degree among all the studied catalysts, as its strong MSI is unfavorable for the sulfidation of Mo species [43]. Compared with CoMo/Al_2O_3 and CoMo/L, the CoMo/LK catalyst exhibits a weaker MSI, which can be attributed to the less Al—OH groups on the surface, moreover, the larger specific surface area and pore size also enhance the accessibility of Mo species, thus its Mo sulfidation degree is relatively higher. The XPS results of the sulfided catalysts agree well with those of H_2-TPR analyses.

Table 3
XPS characterization results of the series of CoMo sulfided catalysts.

Catalysts	CoMo/Al_2O_3	CoMo/L	CoMo/KIT-6	CoMo/LK
$Mo_{sulfidation}$ (%)	25.90	35.26	57.42	45.62

3.1.9. HRTEM characterization

HRTEM is considered to be the most effective technique to characterize the morphology of the active phases via visualizing of the MoS_2 crystallite slabs on the support [21]. Fig. 8 and Table 4 show the representative HRTEM micrographs and the statistical results of different sulfided catalysts, respectively. All the images show the thread-like fringes corresponding to the MoS_2 slabs with 6.1 Å interplanar distances [44]. The particles of the promoter Co species existed on the sulfided catalysts are too small to be visualized, due to the low loading of Co species [45]. To make a quantitative comparison, the lengths and layer numbers of MoS_2 slabs on the sulfided catalysts were measured by the statistical analyses based on about 30 micrographs including at least 300 slabs taken from different parts of each catalyst. The average slab length $\bar{L}$ and the stacking number $\bar{N}$ were calculated according to Eq. (3), where M_i is the slab length or stacking layer number of a stacked MoS_2 unit, and x_i is the number of slabs or stacks in a certain range of length or stacking layer number [46].

$$\bar{L}(\bar{N}) = \frac{\left(\sum_{i=1}^{n} x_i M_i\right)}{\left(\sum_{i=1}^{n} x_i\right)} \quad (3)$$

Table 4
The average length ($\bar{L}$) and average stacking layers ($\bar{N}$) of MoS_2 over the series of CoMo sulfided catalysts.

Catalysts	$\bar{L}$(nm)	$\bar{N}$	f_{Mo}
CoMo/Al_2O_3	3.7	2.1	0.29
CoMo/L	3.8	2.4	0.26
CoMo/KIT-6	4.2	3.1	0.23
CoMo/LK	3.6	2.7	0.30

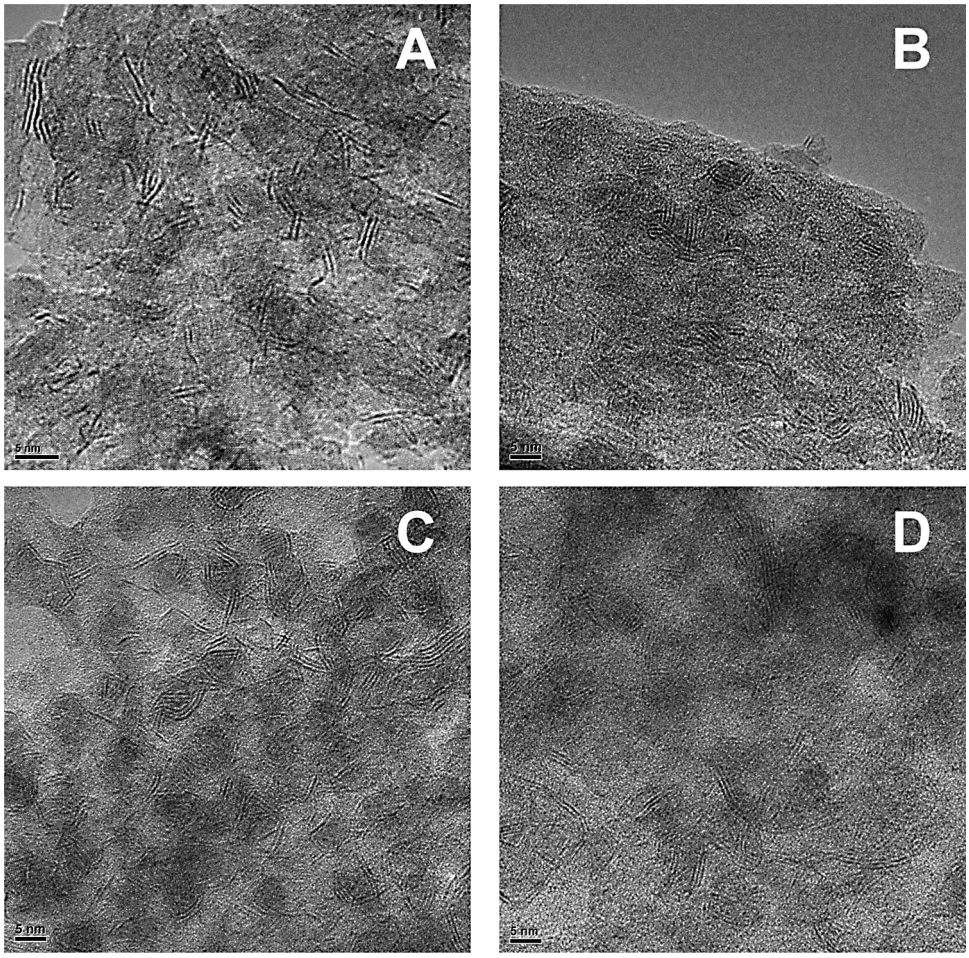

Fig. 8. HRTEM micrographs of the sulfided catalysts. (A) CoMo/Al_2O_3; (B) CoMo/L; (C) CoMo/KIT-6; (D) CoMo/LK.

Based on the statistical results in Table 4, $\bar{N}$ of the MoS_2 slabs over different catalysts increases in the order of CoMo/Al_2O_3 < CoMo/L < CoMo/LK < CoMo/KIT-6, while the $\bar{L}$ value follows the order of CoMo/LK < CoMo/L < CoMo/Al_2O_3 < CoMo/KIT-6. f_{Mo} value shows a trend of CoMo/KIT-6 < CoMo/L < CoMo/Al_2O_3 < CoMo/LK. The dispersion of MoS_2 crystallites is expressed by f_{Mo} (Eq. (2)). For CoMo/LK, f_{Mo} is significantly higher than those of CoMo/L and CoMo/KIT-6, conforming that CoMo/LK has a better MoS_2 dispersion and possesses more active edge sites. The catalysts CoMo/Al_2O_3 and CoMo/L exhibit low stacked degrees and long lengths, indicating that the predominance of low-stacked and big MoS_2 crystallites, which results from that the strong MSI would reduce the accessibility of active centers [47], owing to the steric hindrance. However, the high stacking number (2.7 layers) and relatively short slab length (3.6 nm) over CoMo/LK permit the creations of more available edge and corner sites, allowing the incorporation of more promoter atoms in the structures of type II Co—Mo—S phase [48]. The weak interaction results from Si—O—Mo bands and relatively low amount of the robust Al—O—Mo bands over the siliceous KIT-6 and composite material LK have a great positive effect on morphological and structural property of the metal species [49]. Moreover, weak metal-support interaction is favorable for improving sulfidation of oxidic molybdenum and providing more active sites for the reactants [50], which are beneficial to improving the HDS activities of catalysts.

3.2. Catalytic performance evaluation

3.2.1. Hydrodesulfurization of benzothiophene over CoMo/LK catalyst

In this work, the catalytic performances of a series of supported CoMo catalysts using different support materials including γ-Al_2O_3, zeolite L, KIT-6 and LK for hydrodesulfurization of benzothiophene were evaluated. The evaluation results are displayed in Fig. 9 and Table 5. Fig. 9 demonstrates that the BT conversions over all catalysts increase markedly with decreasing LHSV. Moreover, the BT conversion over CoMo/LK is the highest among all the studied than other catalysts at all LHSVs. The HDS reaction rate constants (K_{HDS}), TOFs, HDS efficiencies, selectivity of products, and HYD/DDS ratios are given in Table 5. The CoMo/LK catalyst exhibits the highest values of the K_{HDS}, TOF and HDS ratio, which are higher than those of CoMo/L, CoMo/KIT-6 and CoMo/γ-Al_2O_3, revealing that the best BT HDS activity among the series of catalysts.

Based on the product distributions of the BT HDS reaction over CoMo/LK in Table 5, the possible HDS reaction network of BT over CoMo/LK was proposed in Fig. 10. Similar to the previous researches [51], BT HDS possibly proceeds through two pathways over the catalyst containing composite material LK. The first pathway is direct desulfurization (DDS), by which BT is desulfurized to form styrene (ST) by hydrogenolysis, then further hydrogenated to ethylbenzene (EB) rapidly. Small amounts of toluene (T) are also obtained, which is the cracking product of EB. This result is in accordance

Table 5
Catalytic activity results for BT HDS reaction over CoMo series of catalysts.

Catalysts	K_{HDS}[a] (10^{-4} mol g^{-1} h^{-1})	TOF[b] (h^{-1})	HDS[c] (%)	Product selectivity[d] (%)			HYD/DDS ratio[e]
				DHBT	EB	T	
$CoMo/Al_2O_3$	9.3	2.7	78.7	31.3	62.5	6.2	0.45
CoMo/L	2.0	0.6	53.2	32.8	59.8	7.4	0.49
CoMo/KIT-6	7.0	2.5	69.8	24.5	74.6	1.0	0.32
CoMo/LK	11.8	3.3	86.9	23.0	69.4	7.7	0.30

[a] The HDS reaction rate constant uses the unit of mol g^{-1} h^{-1}.
[b] Number of the reacted BT molecules per hour and per Mo atom at the edge surface.
[c] HDS ratios of BT on different catalysts with LHSV at 10.0 h^{-1}.
[d] Determined at about 50% of the total BT conversion by changing LHSV.
[e] Obtained dividing HYD by DDS, DDS = (BT + T); HYD = DHBT.

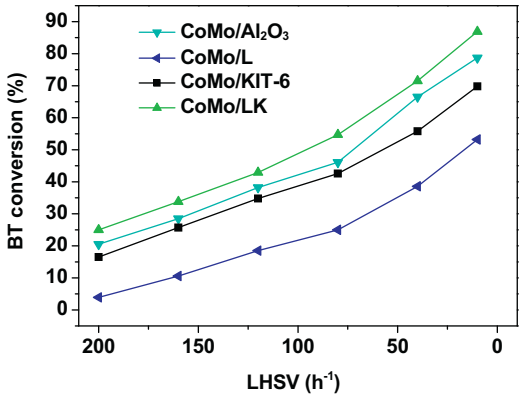

Fig. 9. Catalytic activity results of the BT HDS reaction over the supported CoMo catalysts.

with the previous work by Abe and Bell [52] who also reported the T in the products over Mo_2N as BT HDS catalyst. The second is hydrogenation route (HYD), the aromatic rings of BT is firstly hydrogenated to dihydrobenzothiophene (DHBT) as intermediates, which are then desulfurized to EB. The intermediates such as 2-phenylethylthiol and 2-phenylethanelthiol (in brackets of Fig. 10) would exist according to the report by Wang and Prins [51]. To investigate the individual contributions of the DDS and HYD routes to the overall HDS performance of the series catalysts, the ratio of HYD selectivity to DDS selectivity (HYD/DDS) is obtained by

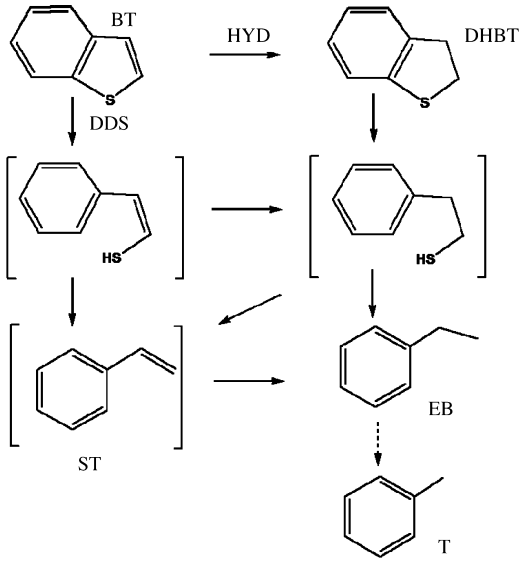

Fig. 10. HDS reaction network of BT over CoMo/LK catalyst.

dividing the (EB + T) selectivity into the DHBT selectivity at the same BT conversion (50%) (Table 5). For this series of catalysts, it can be clearly seen that the DDS route is the preferential pathway in the BT HDS processes. The (EB + T) selectivity over CoMo/LK is the highest among this series of catalysts, demonstrating that the superior hydrogenolysis desulfurization capability of CoMo/LK catalyst. This character also indicates the introduction of the composite support material LK to the catalyst can enhance the HDS performance of catalyst CoMo/LK. The higher selectivity of DDS route can be attributed to the existence of B acid sites and the "edge" active centers.

3.2.2. *Effects of physicochemical properties of the catalysts on their catalytic performances*

The catalytic performances of BT HDS over different catalysts are closely related to the physicochemical properties of the catalysts. As the crucial compositions of catalysts, the properties of support materials and active metals play important roles in HDS reactions. To explain the superior catalytic performance of CoMo/LK in HDS of BT, we attempt to correlate the textural, acid properties of the catalysts, MSI and morphology of the sulfided active metal species with their catalytic performances.

The textural property of catalyst is an important factor for the catalytic conversion of large molecule reactants. Compared with the microporous zeolite L, mesoporous material KIT-6 exhibits prominent textural properties, which are still maintained after the impregnation of active metals (Table 1). The excellent textural properties of CoMo/KIT-6 make great contributions to the dispersion of active metals and the accessibility of active centers in the channels (Table 1). However, Zeolite L, with smaller pore diameter (0.5–0.71 nm), would limit the entrance of BT (0.6 nm) and easily generate diffusion resistance [53]. Moreover, previous researches [54] reported that the open bicontinuous cubic $Ia\bar{3}d$ symmetry structure of CoMo/KIT-6 catalyst provides more favorable mass transfer kinetics than the one-dimension cylindrical pore network of CoMo/L. The introduction of mesoporous template P123 enhances not only the specific surface area (493 m^2 g^{-1}), pore size (5.8 nm) and volume (0.54 cm^3 g^{-1}) of LK, but also the pore structure (cubic $Ia\bar{3}d$). Due to the well interwoven and branched pore structure results from cubic $Ia\bar{3}d$ mesostructure and LTL topology, the derivative catalyst CoMo/LK possesses good diffusion property and mass transfer capability for the reactant BT in the hierarchically channel compared with CoMo/L, which further promotes the interaction between BT and the active sites. Although the conventional HDS catalyst $CoMo/Al_2O_3$ has a relatively large specific surface area, (Table 1) its inter-particle space is not good for mass transfer compared with the bicontinuous cubic $Ia\bar{3}d$ mesostructure.

The acid property of support is one of the important factors for controlling HDS performances. Acidity helps to improve the reaction rates of dealkylation and isomerization of alkyl substitutes, and favors the transformation of the refractory components to more reactive species and thus accelerates the HDS process [55]. Moreover, the acidic supports could also promote the catalytic activity by

the creation of a secondary hydrogenation pathway. The hydrogen atoms can be transferred from the metal particles to the aromatic sulfur-containing molecules that are adsorbed on the acid sites in the vicinity of the metal active sites [56]. Although CoMo/L possesses the highest B and L acid sites in all the catalysts (Table 2), the small pore size and low specific surface area distinctly reduce the accessibility of the acid sites in the narrow channels. In addition, the excessive strong B acid sites and the highest acidity density would lead to a poor stability due to the coke formation [57]. The low utilization of active sites results in a poor BT HDS activity of CoMo/L. The electronically neutral framework of pure silica KIT-6 leads to the derivative catalyst CoMo/KIT-6 only having a small amount of L acid sites, which is insufficient for BT HDS. CoMo/LK catalyst possesses more than twice amounts of total and strong acid sites of CoMo/KIT-6 catalyst. Not only are L acid sites detected, but also some B acid sites are detected on CoMo/LK. Owing to the L basicity in nature of thiophene, the existence of L acid sites on the catalysts could facilitate the adsorption and conversion of thiophene molecules [58]. Meanwhile, B acid sites benefit the C—S and C—C bond cleavages [59]. The mechanism of C—S bond cleavage assisted by acid sites demonstrated that the acid sites might act as a co-catalyst by providing a proton for easier S-atom removal from the ring of reactant molecule. As a consequence, the consecutive elimination step on S^{2-} ions (performing as basic sites) of the active phase is easier. The proton connected with the sulfur can then be transferred to the support in order to regenerate the acid sites [60].

The amount of B acid sites over CoMo/LK was lower than that of CoMo/L, but the excellent textural properties (Table 1) of CoMo/LK made these B acid sites more accessible for the reactants. The existence of B acid sites over CoMo/L and CoMo/LK increased the selectivity of toluene comparing with CoMo/Al_2O_3 and CoMo/KIT-6 which have no B acid sites on the catalyst surfaces (Table 2 and 5). Moreover, the correlation of the HYD/DDS selectivity ratio (Table 5) with the catalyst acidities (Table 2) indicates that the existence of more accessible B acid sites over CoMo/LK improves the DDS activity. The similar phenomenon was also found by W. Welters [59] who investigated the influence of the catalyst acidity on the HDS reaction mechanism of 4,6-dimethyldibenzothiophene (4,6-DMDBT) over CoMo/P/Ti-HMS catalyst. The DDS route was the main reaction route for 4,6-DMDBT on the catalyst. Moreover, both of the activity and selectivity largely depended on the presence of B acid sites as well as on the total amount of B and L acid sites.

CoMo/LK possesses the similar mesostructure to CoMo/KIT-6, while the textural properties including specific surface area and volume are relatively lower due to the in-situ incorporation of L zeolite into the mesoporous frameworks of KIT-6 (Fig. 2 and Table 1). However, the reaction rate constant (K_{HDS}) of BT HDS over CoMo/LK is about 1.7 times as that over CoMo/KIT-6. The existence of more accessible B acid sites over CoMo/LK favors the increase of T content comparing with those of CoMo/KIT-6 and CoMo/Al_2O_3. These differences prove that the suitable acid amount and the synergistic effect of B and L acid sites combining with excellent accessibility over CoMo/LK have a positive effect on the performance of the catalysts for the BT HDS reaction.

Besides the influences of the support properties, the active metals over the catalysts also affect the HDS performances apparently embodied with MSI, sulfurization degree, and the morphology of the supported MoS_2. The dispersion and stacking of MoS_2 are correlated with MSI and the specific surface area. Silanols in molecular framework exhibit weaker MSI than aluminum hydroxyls. Since the pure silicous KIT-6 material exists only silanols which result in the weaker MSI between the metal species and the KIT-6 supports, CoMo/KIT-6 shows the highest sulfurization degree (57.42%). However, the high degree of stacking sulfide slabs (3.1) and some very large MoS_2 crystals lead to a decrease of the edge sites on MoS_2 slabs. Thus, the sulfur elimination via the perpendicular adsorption of the molecules through the S atom is restricted [61]. In addition, the weak MSI over CoMo/KIT-6 would form agglomerated β-$CoMoO_4$ phases which have low HDS activity [38].

Due to the strong MSI between the metals and Al_2O_3 support, CoMo/Al_2O_3 and CoMo/L catalysts show the lower stacking layers of sulfide slabs, 2.1 and 2.4, respectively, which would favor the formation of type I Co—Mo—S phases that expose less edge sites, then they are favorable for the planar adsorption of the reactant molecules through its aromatic rings, but they hamper the perpendicular adsorption through the sulfur atom, thereby resulting in the decrease of HDS activity [62]. Comparably, the acidic synthesis condition decreases the amounts of aluminum hydroxyls of LK. As a result, CoMo/LK shows a weaker MSI compared with CoMo/L. This moderate MSI over CoMo/LK increases the proportion of dispersed octahedral Mo species at the expense of tetrahedral ones. Moreover, it decreases the particle sizes of MoS_2 compared with that of CoMo/KIT-6 (Table 4), thus makes the sulfidation of Mo species on LK easier ($Mo_{sulfidation}$ = 45.62%). Furthermore, the short length (3.6 nm) and the high stacking layers (2.7) of MoS_2 slabs over CoMo/LK favor the formation of more type II Co—Mo—S phases which provide more corner and edge sites (f_{Mo} = 0.3) for the reactants and promote both of planar and perpendicular adsorptions.

In summary, the superior catalytic performance of CoMo/LK catalyst for HDS of BT could be attributed to the synergistic effects of the open pore, desirable textural properties, suitable acidity, moderate MSI and the excellent stacking morphology of Co—Mo—S phases.

4. Conclusions

In this study, a novel kind of micro/mesoporous composite material L-KIT-6 (LK) was successfully synthesized using low cost solid silica–alumina microsphere as the raw materials via a two-step hydrothermal method. The characterization results showed that LK composite possessed the $Ia\bar{3}d$ cubic ordered mesoporous structure similar to the pure silica material KIT-6 and its framework contained the primary and secondary structural building units of microporous zeolite L simultaneously. The textural and acidity properties of the LK composite were improved compared with those of zeolite L and mesoporous KIT-6. LK-supported CoMo catalyst was prepared and characterized. The catalytic performance evaluation results showed that CoMo/LK exhibited the highest BT HDS activity among all the studied catalysts and the TOF of BT HDS on CoMo/LK was about 1.3 times as much as that on CoMo/Al_2O_3 because of the perfect combination of open-framework structure, desirable textural properties, suitable acidity, moderate MSI and the excellent stacking morphology of Co—Mo—S phase. A possible reaction network for BT HDS over CoMo/LK catalyst was proposed. Moreover, the synergy of B acid sites and the “edge” active centers on CoMo/LK promoted the selectivity of DDS route. As a result, the outstanding physicochemical properties endowed the LK micro/mesoporous composite to be a promising support material for HDS.

Acknowledgements

The authors acknowledge the financial supports from the National Natural Science Foundation of China (nos. 21073235 and 21276277), Opening Project of Guangxi Key Laboratory of Petrochemical Resource Processing and Process Intensification Technology (2012K01) and CNPC Key Research Project.

Appendix A. Supplementary data

Supplementary data associated with this article can be found, in the online version, at http://dx.doi.org/10.1016/j.apcatb.2014.10.078.

References

[1] C. Song, X. Ma, Appl. Catal., B: Environ. 41 (2003) 207–238.
[2] S.A. Al-Bogami, H.I. de Lasa, Fuel 108 (2013) 490–501.
[3] W. Welters, G. Vorbeck, H. Zandbergen, L. Van de Ven, E. Van Oers, J. De Haan, V. De Beer, R. Van Santen, J. Catal. 161 (1996) 819–828.
[4] L. Kaluža, D. Gulková, Z. Vít, M. Zdražil, Appl. Catal., B: Environ. 162 (2015) 430–436.
[5] A. Dugulan, J. van Veen, E. Hensen, Appl. Catal., B: Environ. 142 (2013) 178–186.
[6] O.Y. Gutiérrez, T. Klimova, J. Catal. 281 (2011) 50–62.
[7] L. Kaluža, D. Gulková, O. Šolcová, N. Žilková, J. Čejka, Appl. Catal., A: Gen 351 (2008) 93–101.
[8] C.A. Ulín, J.A. De Los Reyes, J. Escobar, M.C. Barrera, M.A. Cortés-Jacome, J. Phys. Chem. Solids 71 (2010) 1004–1012.
[9] J. Álvarez-Rodríguez, A. Guerrero-Ruiz, I. Rodríguez-Ramos, A. Arcoya-Martín, Catal. Today 107 (2005) 302–309.
[10] M. Taniguchi, D. Imamura, H. Ishige, Y. Ishii, T. Murata, M. Hidai, T. Tatsumi, J. Catal. 187 (1999) 139–150.
[11] J. Jiang, J.L. Jorda, J. Yu, L.A. Baumes, E. Mugnaioli, M.J. Diaz-Cabanas, U. Kolb, A. Corma, Science 333 (2011) 1131–1134.
[12] T.-W. Kim, F. Kleitz, B. Paul, R. Ryoo, J. Am. Chem. Soc. 127 (2005) 7601–7610.
[13] K. Soni, B. Rana, A. Sinha, A. Bhaumik, M. Nandi, M. Kumar, G. Dhar, Appl. Catal., B: Environ. 90 (2009) 55–63.
[14] R. Srivastava, M. Choi, R. Ryoo, Chem. Commun. (2006) 4489–4491.
[15] Y. Di, Y. Yu, Y. Sun, X. Yang, S. Lin, M. Zhang, S. Li, F.-S. Xiao, Microporous Mesoporous Mater. 62 (2003) 221–228.
[16] Y. Sun, R. Prins, Angew. Chem. Int. Ed. 47 (2008) 8478–8481.
[17] W. Fu, L. Zhang, T. Tang, Q. Ke, S. Wang, J. Hu, G. Fang, J. Li, F.-S. Xiao, J. Am. Chem. Soc. 133 (2011) 15346–15349.
[18] D. Zhang, A. Duan, Z. Zhao, C. Xu, J. Catal. 274 (2010) 273–286.
[19] Q. Huo, Y. Gong, T. Dou, Z. Zhao, H. Pan, F. Deng, Energy Fuels 24 (2010) 3764–3771.
[20] Z. Luan, M. Hartmann, D. Zhao, W. Zhou, L. Kevan, Chem. Mater. 11 (1999) 1621–1627.
[21] G. Berhault, M. Perez De la Rosa, A. Mehta, M.J. Yácaman, R.R. Chianelli, Appl. Catal., A: Gen. 345 (2008) 80–88.
[22] W. Lai, W. Song, L. Pang, Z. Wu, N. Zheng, J. Li, J. Zheng, X. Yi, W. Fang, J. Catal. 303 (2013) 80–91.
[23] Y. Fan, H. Xiao, G. Shi, H. Liu, Y. Qian, T. Wang, G. Gong, X. Bao, J. Catal. 279 (2011) 27–35.
[24] E. Hensen, P. Kooyman, Y. Van der Meer, A. Van der Kraan, V. De Beer, J. Van Veen, R. Van Santen, J. Catal. 199 (2001) 224–235.
[25] Y.S. Ko, W.S. Ahn, Powder Technol. 145 (2004) 10–19.
[26] C. Montes de, C.A.d. Luz Villa de, P.M. Ramírez-Corredores, Appl. Catal., A: Gen 197 (2000) 151–156.
[27] V. Umamaheswari, M. Palanichamy, V. Murugesan, J. Catal. 210 (2002) 367–374.
[28] M. Tsapatsis, M. Lovallo, T. Okubo, M.E. Davis, M. Sadakata, Chem. Mater. 7 (1995) 1734–1741.
[29] A. Vinu, N. Gokulakrishnan, V.V. Balasubramanian, S. Alam, M.P. Kapoor, K. Ariga, T. Mori, Chem. Eur. J. 14 (2008) 11529–11538.
[30] Y. Han, S. Wu, Y. Sun, D. Li, F.-S. Xiao, J. Liu, X. Zhang, Chem. Mater. 14 (2002) 1144–1148.
[31] T. Jiang, L. Qi, M. Ji, H. Ding, Y. Li, Z. Tao, Q. Zhao, Appl. Clay. Sci. 62 (2012) 32–40.
[32] R. Bertram, U. Lohse, W. Gessner, Z. Anorg. Allg. Chem. 567 (1988) 145–152.
[33] Y. Liu, W. Zhang, T.J. Pinnavaia, Angew. Chem. Int. Ed. 40 (2001) 1255–1258.
[34] J.A. Pieterse, S. Veefkind-Reyes, K. Seshan, L. Domokos, J.A. Lercher, J. Catal. 187 (1999) 518–520.
[35] J. Marques, I. Gener, P. Ayrault, J. Bordado, J. Lopes, F. Ramôa Ribeiro, M. Guisnet, Microporous Mesoporous Mater. 60 (2003) 251–262.
[36] S. Damyanova, A. Spojakina, K. Jiratova, Appl. Catal., A: Gen. 125 (1995) 257–269.
[37] D.C. Vermaire, P.C. van Berge, J. Catal. 116 (1989) 309–317.
[38] D. Valencia, T. Klimova, Catal. Today 166 (2011) 91–101.
[39] L. Peña, D. Valencia, T. Klimova, Appl. Catal., B: Environ. 147 (2014) 879–887.
[40] L.Y. Lizama, T.E. Klimova, J. Mater. Sci. 44 (2009) 6617–6628.
[41] J. Muijsers, T. Weber, R. Vanhardeveld, H.W. Zandbergen, J. Niemantsverdriet, J. Catal. 157 (1995) 698–705.
[42] Y. Fan, H. Xiao, G. Shi, H. Liu, X. Bao, Energy Environ. Sci. 4 (2011) 572–582.
[43] M.S. Rana, J. Ramírez, A. Gutiérrez-Alejandre, J. Ancheyta, L. Cedeño, S. Maity, J. Catal. 246 (2007) 100–108.
[44] T.F. Hayden, J. Dumesic, J. Catal. 103 (1987) 366–384.
[45] D. Zuo, D. Li, H. Nie, Y. Shi, M. Lacroix, M. Vrinat, J. Mol. Catal., A: Chem. 211 (2004) 179–189.
[46] S. Eijsbouts, J. Heinerman, H. Elzerman, Appl. Catal., A: Gen. 105 (1993) 53–68.
[47] T. Zepeda, B. Pawelec, J. Fierro, T. Halachev, Appl. Catal., B: Environ. 71 (2007) 223–236.
[48] R. Candia, O. Sorensen, J. Villadsen, N.-Y. Topsøe, B. Clausen, H. Topsøe, Bull. Soc. Chim. Belg. 93 (1984) 763–773.
[49] Y. Okamoto, K. Ochiai, M. Kawano, K. Kobayashi, T. Kubota, Appl. Catal., A: Gen. 226 (2002) 115–127.
[50] W. Han, P. Yuan, Y. Fan, H. Liu, X. Bao, J. Mater. Chem. 22 (2012) 12121–12127.
[51] H. Wang, R. Prins, Appl. Catal., A: Gen. 350 (2008) 191–196.
[52] H. Abe, A.T. Bell, Catal. lett. 18 (1993) 1–8.
[53] L.D. Rollmann, P.A. Howley, D.N. Mazzone, H.K.C. Timken, Ind. Eng. Chem. Res. 34 (1995) 3970–3973.
[54] K. Schumacher, M. Grün, K.K. Unger, Microporous Mesoporous Mater. 27 (1999) 201–206.
[55] G. Pérot, Catal. Today 86 (2003) 111–128.
[56] S.D. Lin, M.A. Vannice, J. Catal. 143 (1993) 539–553.
[57] S. Sahoo, N. Viswanadham, N. Ray, J. Gupta, I. Singh, Appl. Catal., A: Gen. 205 (2001) 1–10.
[58] G. Kim, R.F. Wormsbecher, EP Pat: 0609971, 1993-01-27, 1993.
[59] W. Welters, V. De Beer, R. Van Santen, Appl. Catal., A: Gen. 119 (1994) 253–269.
[60] B. Pawelec, J.L.G. Fierro, A. Montesinos, T.A. Zepeda, Appl. Catal., B: Environ. 80 (2008) 1–14.
[61] H. Topsøe, Appl. Catal., A: Gen. 322 (2007) 3–8.
[62] H. Wang, R. Prins, J. Catal. 258 (2008) 153–164.